Intercellular DNA transfer mediated by migrasomes propagates genome instability

Yi Li[1#], Yihan Tang[1,2#], Guojun Ye[1,3], Chunzhuo Liu[1,4], Yide He[1], Chunyu Song[1,3], Weiping Chang[1], Yuwei Huang[5], Wei-ke Ji[6,7], and Lin Deng[1*]

[1]Shenzhen Bay Laboratory, Shenzhen, Guangdong, 518132, China;

[2]School of Life Science and Technology, Harbin Institute of Technology, Harbin, Heilongjiang, 150006, China;

[3]Department of Biochemistry and Molecular Biology, Capital Medical University, Beijing, 100069, China;

[4]Department of Chemistry, Southern University of Science and Technology, Shenzhen, Guangdong, 518055, China;

[5]School of Basic Medical Sciences, Translational Medicine Institute, Xi'an Jiaotong University, Xi'an 710049, China;

[6]Department of Biochemistry and Molecular Biology, School of Basic Medicine, Tongji Medical College, Huazhong University of Science and Technology, Wuhan, Hubei, 430030, China;

[7]Cell Architecture Research Institute, Huazhong University of Science and Technology, Wuhan, Hubei, 430030, China;

[#]These authors contribute equally

[*]Corresponding author. Email: denglin@szbl.ac.cn (L.D.)

One sentence summary: Intercellular DNA transfer via migrasome-mediated chromocytosis propagates genome instability and drives cancer genome evolution.

Abstract

Genome instability drives tumor evolution through incremental mutations and catastrophic events such as chromothripsis. Despite significant advances, the diversity and underlying mechanisms of genome instability remain insufficiently understood. Here, we identify a previously unrecognized form of genome instability termed "chromocytosis", in which chromosome bridge breakage during mitosis causes permanent loss of chromatin fragments from daughter cells. These extracellular fragments could be transferred into neighboring cells via migrasomes and compromise the genome integrity of the recipient cells. This intercellular chromatin transfer is conserved across cell types and observed *in vivo* in mouse tumor models and multiple human cancers. Disruption of migrasome formation attenuates chromocytosis and its genomic consequences. Our work establishes chromocytosis, the migrasome-mediated intercellular transfer of chromatin fragments, as a potent mechanism for propagating genomic instability and driving tumor evolution.

Introduction

Genome instability is a critical driver of human tumor evolution and shapes the complex genomic landscape of cancer cells (*1-4*). Traditionally, tumor evolution has been viewed as the gradual accumulation of mutations (*5*), where a multitude of simple errors during DNA replication culminate in a large, intricate, and chaotic genome (*6, 7*). These mutations can occur throughout the genome due to various factors, including genetic alterations that stimulate or disrupt cell cycle checkpoints, thereby promoting further genome instability and facilitating tumor growth (*1, 7, 8*). However, recent pan-cancer genome-wide analyses have revealed the complex nature of many human tumor genomes, marked by localized large-scale rearrangements on one or several chromosomes (*9-11*). These rearrangements lead to aneuploidy and are frequently attributed to singular catastrophic events, such as kataegis during chromosome breakage-fusion-bridge (BFB) cycles (*12*) and chromothripsis in micronuclei (*13, 14*). These events promote the rapid evolution and complexity of cancer genome (*15-17*).

Chromosome bridges, a major form of genome instability, often result from DNA replication stress, telomere fusion, or DNA damage during cell division (*18-20*). As a cell enters mitosis with dicentric chromosomes, centromeres are pulled in opposite directions, forming a bridge between the chromosomes. TRF2 (telomeric repeat-binding factor 2), a component of shelterin complex, plays a crucial role in maintaining telomere integrity and preventing chromosomal fusions. Deficiency of TRF2 exacerbates telomere fusion and breakage, thereby promoting the formation of chromosome bridges (*21, 22*). The bridge can persist until the centrosomes are sufficiently separated, leading to double-strand breaks. These breaks initiate the BFB cycle, which drives further rearrangements and results in the formation of micronucleus and chromothripsis (*23-25*). Defects in nuclear envelope assembly, along with the nuclear distortions in micronuclei or chromosome bridges, have been linked to chromothripsis (*26-28*). The impact of chromosome bridge breakage, as a localized DNA damage event, and its influence on cell fate remain to be elucidated.

Intercellular transfer of materials plays a crucial role in cell-to-cell communication, tissue homeostasis, and disease progression, including cancer (*29*). It can be achieved through extracellular vesicles (EVs), tunneling nanotubes (TNTs), and migrasomes. EVs, including exosomes and microvesicles, facilitate intercellular communication by mediating the exchange of proteins, RNAs, and metabolites (*30*). Tunneling nanotubes (TNTs) create direct cytoplasmic continuity between cells to selectively ferry vesicles and organelles (*31*). In nervous system, TNTs mediate the movement of α-synuclein aggregates mainly from neurons to microglia and mitochondria preferentially from microglia to stressed neurons, coupling pathologic protein aggregate clearance with metabolic rescue (*32*). Migrasomes, a new type of extracellular vesicular organelle (*33*), could regulate mitochondrial homeostasis via mitocytosis (*34*), in addition to RNA and proteins transfer (*35, 36*). However, the role of migrasomes in genome instability remains unexplored. Regarding to DNA, horizontal gene transfer allows bacteria to acquire new genetic material from other bacteria and enables adaptive evolution (*37*). Meanwhile, eukaryotic cells could obtain foreign DNA passively through viral infections. However, whether DNA could be transferred between human cells remains unexplored.

In this study, we identify chromocytosis, a process in which chromosome bridge breakage leads to loss of chromatin fragments that are captured by migrasomes and horizontally transferred to neighboring cells, thereby propagating genome instability.

Results

Breakage of chromosome bridges causes chromocytosis

The prevailing model suggests that the breakage of chromosome bridges typically leads to a binary outcome, resulting in the loss or gain of DNA fragments from the involved chromosomes (*14, 38*). These imbalanced chromosomes are subsequently segregated into the two daughter cells. To further elucidate this process, TRF2-DN (dominant-negative TRF2) was inducibly expressed in human retinal pigmented epithelial (RPE-1) cells with p53 knockout to efficiently generate chromosome bridges (Fig. 1, A to C), marked by GFP-tagged BAF (barrier-to-autointegration factor) in conjunction with RFP-tagged histone 2B (RFP-H2B) to label chromosomal DNA. We used extensive time-lapse imaging to monitor the dynamics and fate of chromosome bridges. During cell division, chromosome bridges could persist into interphase and stretched due to cell migration. The majority of the bridges underwent simple breakage and retraction of the chromatin back to the cell bodies (Fig. 1D, top panels and movie S1). Surprisingly, some bridges failed to retract all their DNA after breakage, leaving a fragment of chromatin outside of the daughter cells (Fig. 1D, bottom panels and movie S2). This results in the permanent loss of genetic material from the daughter cells. We termed this phenomenon "chromocytosis", a previously unrecognized form of genome instability (Fig. 1E).

Among the observed bridges, about 10% of them underwent chromocytosis (Fig. 1F). Furthermore, compared to the bridges with simple breakage, chromocytotic bridges showed significantly greater extension in size (from 219.50 ± 6.83 μm to 396.40 ± 10.42 μm on average, Fig. 1G) and longer lifetime, the time from mitosis to bridge breakage (from 7.11 ± 0.36 h to 11.64 ± 0.44 h on average) (Fig. 1H). In addition to TRF2-DN, low-dose ICRF-193, a topoisomerase II inhibitor, was used to induce chromosome bridges by interfering with chromosome decatenation during mitosis (*39*) (fig. S1A). In contrast to DMSO treatment, ICRF-193 triggered chromocytosis in ~18% chromosome bridges (fig. S1, B and C, movie S3 and S4). The chromocytotic bridges under this condition also exhibited longer lengths and lifetimes (fig. S1, D and E).

Because cell adhesion is essential for cytokinesis and chromatin dynamics (*40, 41*), we investigated whether cell adhesion is required for chromocytosis by growing cells on plates coated with or without fibronectin (FN). Compared to the uncoated control, cells on FN-coated plate showed more chromosome bridges after TRF2-DN induction, possibly due to increased survival (Fig. 1I). More importantly, the frequency of chromocytosis nearly doubled (Fig. 1J), suggesting that cell adhesion could promote chromocytosis. Therefore, the subsequent experiments were performed under conditions with FN coating.

In addition, we examined the role of cell motility and mechanical forces in chromocytosis, as they could stretch a bridge across its length for breakage (*42*). Consistent with previous report (*42*), treatment of ML7, an inhibitor of myosin activation, markedly reduced the length and increased the lifetime of chromosome bridges (fig. S2, A and B). Accordingly, the rate of chromocytosis was dropped from 26.57 ± 2.14% to 5.46 ± 0.72% (fig. S2C). These results were confirmed by the treatment of Latrunculin A (Lat-A), an actin assembly inhibitor (fig. S2, D to F). Lat-A appeared to suppress chromocytosis more strongly than ML7. Together, these data establish a critical role for actomyosin contractility and cell motility in chromosome bridge breakage and chromocytosis.

Migrasomes are required for chromocytosis

During cell migration, membrane-bound organelles called migrasomes could form on the tips or intersections of the retraction fibers (*33*), participating in various intercellular biological functions (*43, 44*). When a chromosome bridge was generated, a thread of retraction fiber marked by RFP-TSPAN4 was always stretched with it, surrounded by bundles of shorter retraction fibers (fig. S3A). Once vesicular migrasomes started to grow, the chromosome bridge became fragmented but still wrapped by RFP-TSPAN4 (fig. S3B). The chromatin fragments from bridge breakage appeared to shrink along within the retraction fiber and were encapsulated in migrasomes (fig. S3C, movie S5). In addition to human RPE-1 cells, chromocytosis in mouse fibroblast L929 cells also triggered the encapsulation of chromatin fragments in migrasomes (fig. S3, D and E, and movie S6). Correlative light and electron microscopy (CLEM) confirmed that DNA fibers were encapsulated in bubbled structures with 1-3 μm in length (Fig. 2A, fig. S3F, and movie S7 to S9), likely migrasomes.

The involvement of migrasomes in chromocytosis was confirmed by genetic ablation of migrasome components. Knocking out *TSPAN4* (*TSPAN4 KO*) using CRISPR/Cas9 (fig. S4, A to C) significantly reduced the number of migrasomes (Fig. 2B and fig. S4D)， as previously reported (*45, 46*). Intriguingly, the rate of chromocytosis dropped from ~29% in wild type (*WT*) to ~9% in *TSPAN4 KO* (Fig. 2C, fig. S4E), although the length and lifetime of chromosome bridges showed no difference between *WT* and *TSPAN KO* (Fig. 2, D and E). Similarly, when TSPAN7, another migrasome component gene was knocked out (fig. S4, F to H), the number of migrasome and chromocytosis was significantly reduced (fig. S4, I to K), whereas the bridge length and lifetime were unaltered (fig. S4, L and M). These results suggested that migrasomes play crucial roles during chromocytosis.

To obtain direct biochemical evidence that migrasomes encapsulate chromocytotic DNA, we purified migrasomes through density gradient centrifugation as reported (*47*) (Fig. 2F). Migrasomes from DMSO treated cells showed dim soluble GFP-BAF signal and negative DNA staining. In contrast, migrasome from DOX-induced chromocytotic cells exhibited strong GFP-BAF and DNA signals (Fig. 2G). There was 7-fold (1.93 ± 0.35% versus 14.98 ± 2.08% on average) increase in DNA positive migrasomes (Fig. 2H). Next-generation sequencing of the chromocytotic DNA revealed that DNA peaks could be mapped to almost all chromosomes, and chromosome 10 showed the highest value followed by chromosomes 13, 20 and 21 (fig. S5, A and B). The lengths of DNA fragments demonstrated a normal distribution, ranging from 10 Kb to 1 Mb with a peak at 100 Kb (Fig. 2I). Surprisingly, the DNA peaks reproducibly showed biased clustering at centromeric regions (Fig. 2J and fig. S5, B and C), although the chromosome bridges were induced by telomere fusion. Our data indicate that chromosome bridges break preferentially at centromeric regions. The mechanism underlying this site-specific fragility warrants future investigation. Together, our imaging and biochemical purification establish migrasomes as the direct carriers of extracellular chromocytotic DNA.

Beyond chromocytosis, migrasomes also mediate mitocytosis of damaged mitochondria (*34*). To investigate whether these two processes have crosstalk, mitochondria in migrasomes were examined using mito-tracker in RPE-1 cells with inducible TRF2-DN (fig. S6A). Compared to the control, chromocytosis did not alter the overall migrasome number and the number of mitochondria positive (mito+) migrasomes (fig. S6, B and C), although it significantly increased the number of DNA positive (DNA+) migrasomes (fig. S6D). Meanwhile, carbonyl cyanide 3-chlorophenylhydrazone (CCCP), an inhibitor of oxidative phosphorylation (*34*), was used to induce mitocytosis (fig. S6E), which indeed increased mito+ migrasomes (fig. S6F). However, the

overall migrasome number and DNA+ migrasomes were not significantly affected (fig. S6, G and H). These findings demonstrate that chromocytosis and mitocytosis are two independent processes.

Intercellular transfer of chromocytotic DNA causes genome instability

To explore the physiological function of chromocytosis, we tracked the fate of the extracellular chromocytotic DNA using time-lapse imaging. Most fragments stayed at the site of chromosomal breakage for tens of hours, while a subset could be engulfed by neighboring cells (Fig. 3A and movie S10). Intriguingly, a granddaughter of the cell undergoing chromocytosis could retrace its path on its retraction fibers to phagocytose the chromocytotic DNA (fig. S7A and movie S11). We termed this new type of chromocytosis-mediated phagocytosis "**chromocytophagy**" (Fig. 3B). Importantly, chromocytophagy achieved the intercellular DNA transfer. CLEM imaging of the chromocytophagic DNA in the recipient cell revealed collapsed membrane structures surrounding the DNA fragments (Fig. 3C and movie S12), suggesting possible degradation by lysosomes as previously described (*33*). To further confirm the intercellular DNA transfer, we designed a co-culturing assay in which recipient cells were marked by GFP-BAF and the donor cells with inducible TRF2-DN were labeled with RFP-BAF. Dual-colour imaging after 48 hours chromosome bridge induction identified RFP-BAF signals in GFP-BAF cells, either in cytosol or nucleus **(**Fig. 3D**)**. Compared to the DMSO control, chromocytosis induced nearly 7-fold increase of GFP cells with RFP signal **(**Fig. 3E**)**. We observed that chromocytotic DNA persisted in recipient cells and was transmitted through multiple cell divisions (fig. S7, B and C, and movie S13). Notably, the division of cells post chromocytosis (fig. S7A) or chromocytophagy (fig. S7B) indicated that chromocytosis *per se* might not necessarily cause cell cycle arrest or cell death in either donor or recipient cells.

Next, we monitored the genome integrity of the recipient cells to investigate the long-term effect of chromocytosis. In the recipient cells alone (GFP-BAF only) or the co-culture without chromocytosis induction (Mix + DMSO), the basal level of micronuclei (MN) and chromosome bridges remained at about 1% over a 7-day period. However, the co-culture with chromocytophagy (Mix + DOX) showed a steady increase in genome instability (from 0.82 ± 0.28% at day 1 to 6.83 ± 0.35% at day 7) and the percentage of cells with GFP-BAF foci **(**Fig. 3F and fig. S8, A and B**)**, indicating that intercellular DNA transfer directly compromises genome integrity in the recipient cells. To further validate this hypothesis, migrasomes were purified from RFP-BAF cells without TRF2-DN induction (normal migrasomes) or with induction (chromocytotic migrasomes), and incubated with the GFP-BAF recipient cells. Compared to the mock (PBS buffer) treatment, incubation of normal migrasomes showed almost no effect, whereas the treatment of chromocytotic migrasomes increased genome instability from 1.60 ± 0.20% to 7.97 ± 0.23% on average (Fig. 3G and fig. S8, C and D**)**. Accordingly, recipient cells and the chromocytotic DNA in them exhibited higher levels of DNA damage evidenced by Serine 139 phosphorylation in Histone 2A (γ-H2AX) (Fig. 3H and fig. S8E). Together, these findings demonstrated that intercellular transfer of chromocytotic DNA results in genome instability in the recipient cells. Thus, chromocytosis serves not only as a mechanism for genetic loss in donor cells but also as a conduit for genotoxic stress in the recipient population.

Chromocytosis occurs in mouse tumor model and human cancers

Chromocytosis induces genome instability which plays an important role in tumor growth. To investigate the pathological role of chromocytosis *in vivo*, we employed the mouse 4T1 breast cancer model. First, the TRF2-DN induction cassette was introduced into the 4T1 cells (fig. S9A). Chromocytosis was observed after chromosome bridge breakage (fig. S9B, and movie S14). Meanwhile, TSPAN4 was knocked out in WT (fig. S9, C to E), followed by introduction of TRF2-DN. Then, subcutaneous injection of 4T1 WT or TSPAN KO cells with or without TRF2-DN was performed in BALB/c nude mice (n=6 for each group). Oral administration of DOX (20 mg/kg) was conducted every two days for all four groups at day 8 when tumor size reached ~100 mm^3 (Fig. 4A). DOX administration itself did not cause tumor growth defect (fig. S9F). Tumor growth including size and weight was closely monitored (Fig. 4, B to D). In WT background, TRF2 DN induction reduced tumor growth, suggesting a negative role of chromosome bridges in proliferation. Consistent with previous report (*48*), TSPAN4 KO reduced tumor growth. Intriguingly, the TRF2-DN-induced growth defect was almost completely abolished by TSPAN4 KO, suggesting that growth defect caused by genome instability including chromocytosis might depend on migrasomes. To assess whether chromocytosis occur in tumor microenvironment, histological analysis was performed on tumor tissue sections stained with WGA (wheat germ agglutinin) for migrasomes/membrane(*49*) and Hoechst for DNA. Events of chromocytosis, extracellular DNA wrapped by WGA staining, were almost exclusively detected in samples with TRF2-DN expression. In contrast, nearly none chromocytosis events were detected in TSPAN4 KO samples (Fig. 4, E and F, and fig. S9G). These *in vivo* results confirmed the importance of migrasomes in chromocytosis.

Furthermore, we extended the analysis to human cancer samples to explore the clinical relevance of chromocytosis. A total of 96 samples covering 16 different peritumoral tissues and cancer types and stages were subject to DNA and WGA staining before imaging (fig. S9H). Across these cancer types, chromocytosis events were identified most in ESCC (esophageal squamous cell carcinoma) and Lymphoma (Fig. 4G), followed by bladder cancer. However, chromocytosis events were hardly observed in skin, brain and ovary cancers (Fig. 4H). Notably, chromocytosis events did not correlate with tumor stage or grade (fig. S9, I and J), indicating that chromocytosis might be a sporadic or recurrent event during tumorigenesis or tumor growth. Altogether, these data provided direct evidence that chromocytosis could occur in mouse tumor models and clinical samples of human cancers.

Many factors could contribute to the varied frequencies of chromocytosis among cancer types (Fig. 4H). One of them might be cell motility, as chromocytosis requires cell migration (fig. S2, C and F). This raised the question whether chromocytosis occurs in non-migratory tumor cells. To address this, non-migratory HeLa (human cervical cancer) cells were examined. Chromosome bridges induced by TRF2-DN in HeLa cells showed three types of morphology which we classified as dumbbell, semi-, and full bridge (fig. S10A). Dumbbell bridges dominated in HeLa cells (fig. S10B), whereas majority in RPE-1 cells were full bridges (fig. S10C). More importantly, retraction fibers, migrasomes and chromocytosis were hardly observed in HeLa cells. In most cases, chromosome bridges persisted between the daughter cells as dumbbells without breakage, likely due in part to short distance and lack of actomyosin force. The persistent bridges might undergo breakage due to mitosis followed by micronucleation but without chromocytosis (fig. S10D, and movie S15). Therefore, cell migration could serve as a valuable indicator to assess chromocytosis in different cancers.

Discussion

Genome instability is a hallmark of cancer, yet how it propagates across cell populations remains incompletely understood. Here, we identify chromocytosis, a migrasome-mediated process that enables the horizontal transfer of chromatin fragments following mitotic bridge breakage. This process may promote tumor heterogeneity by disseminating genomic rearrangements among cell populations, complementing other mechanisms of rapid genome reorganization such as chromothripsis and kataegis (*12, 50*). Beyond corrupting neighboring cancer cells, chromocytosis could also serve as a "genetic sabotage" mechanism, destabilizing the genomes of surrounding normal stromal or immune cells, thereby fostering a permissive microenvironment for tumor expansion.

The process of chromocytosis is mechanistically linked to migrasome biogenesis. Genetic disruption of *TSPAN4* or *TSPAN7*, proteins essential for migrasome formation (*46*), substantially reduced the frequency of chromocytosis. The finding that chromocytotic DNA is enriched in centromeric regions suggests a non-random pattern of chromosome bridge fragmentation. This establishes a new cargo category for migrasomes, which were previously known to transfer RNA, proteins, and organelles (*34, 51*). Chromocytosis functions independently of mitocytosis (*34*), indicating specificity in the cargo selection of migrasomes. The detection of chromocytosis in human cancer samples, particularly in ESCC and lymphoma, underscores its clinical relevance. Beyond its role in intercellular communication, a functional implication of chromocytosis is its potential role as a source of cell-free DNA (cfDNA). The prevailing models attribute cfDNA primarily to apoptosis or necrosis (*30*). Our data indicate that chromocytosis can occur in the absence of observable cell death, providing an alternative, cell death-independent origin for cfDNA.

Our discovery of chromocytosis opens several new avenues of inquiry. First, the molecular mechanisms governing the packaging of chromatin into migrasomes are completely unknown. Second, given the potent immunostimulatory nature of cytosolic DNA, it will be critical to determine whether chromocytotic DNA activates innate immune pathways such as cGAS-STING (*52*). Therapeutically, our data raise the possibility that inhibiting migrasome formation could modulate genome instability. Finally, it is valuable to explore whether chromocytosis occurs in other contexts of genome instability such as micronucleation (*26*), DNA damage (*53*), or the processing of extrachromosomal DNA (ecDNA) (*54, 55*) and what physiological or pathological roles it might play in these scenarios.

In summary, chromocytosis represents a migrasome-facilitated route for chromatin transfer that may promote tumor evolution through both cell-autonomous and microenvironmental mechanisms. Its independence from cell death further broadens the potential sources of cfDNA. Understanding the regulation and consequences of chromocytosis could open new avenues for limiting tumor heterogeneity and refining cfDNA-based diagnostics.

Materials and Methods

Cell culture

HeLa, HEK293FT, L929 and 4T1 cell lines were maintained in Dulbecco's Modified Eagle Medium (DMEM). hTERT RPE-1 cells were cultured in DMEM/Nutrient Mixture F-12 medium.

All cell lines were maintained in complete medium supplemented with 10% fetal bovine serum (FBS) and 1% penicillin/streptomycin (Gibco) at 37℃ in a humidified atmosphere with 5% CO_2. Mycoplasma contamination was regularly monitored. All cell lines used in this study are listed in Table S1.

DNA construction

TRF2-DN (dominant-negative) and TSPAN4 were amplified from cDNA, then cloned into pDONR223 using BP Clonase (Thermo Fisher Scientific, Cat. #11791019) to generate pENTR223 entry vectors. pENTR223-TRF2-DN was recombined into pCW57.1-V5-DEST via LR Clonase II Enzyme (Thermo Fisher Scientific, Cat. #11791019) to generate TetON-TRF2-DN expression vector. pENTR223-TSPAN4 was recombined into pLVpuro-DEST-CMV-RFP to generate pLVpuro-DEST-CMV-RFP-TSPAN4 via LR Clonase II Enzyme. H2B-BFP was introduced into the pLenti-CMV-neoR via AscI and PacI restriction sites. pLenti-NeoR-EGFP-BAF and RFP-H2B vectors were kindly provided by David Pellman (Harvard Medical School/HHMI). All DNA constructs used in this study were confirmed by Sanger sequencing, and listed in Table S2.

To construct dual sgRNA expression vectors for the CRISPR-Cas9 system, PCR-amplified fragments, containing sgRNA sequences flanked by the dual H1 and U6 promoters, were cloned into the pLenti-CRISPRv2-2×Scaffold vector (a modified version of pLenti-CRISPRv2) via Esp3I (type II DNA endonuclease) recognition sites. The sgRNA target sequences for the genes of interest in this study are listed in Table S3.

Virus packaging and stable cell line generation

Lentiviral particles were generated by co-transfecting HEK293FT cells with 1.5 μg of ps-PAX2, 1.2 μg of pMD2.G, and 2.4 μg of target viral vector using Lipofectamine 2000 (Invitrogen, Cat. #11668019) according to the manufacturer's instructions. After an overnight incubation, the medium was replaced with 3 mL of fresh medium. The supernatant was collected at 48 and 72 hours post-transfection and filtered through a 0.45 μm syringe filter. The collected supernatant, containing lentiviral particles, was used for the infection of target cells. Prior to infection, the viral supernatant was supplemented with polybrene (6 μg/mL) to enhance transduction efficiency. The cells were incubated with the viral supernatant overnight to allow for infection.

RPE-1 *TP53-/-* cells stably expressing TetOn-TRF2-DN-V5, GFP-BAF, RFP-BAF, or RFP-TSPAN4 were selected with 750 μg/mL neomycin (G418) for two weeks or 10 μg/mL puromycin for a week, L929 cells co-expressing GFP-BAF and RFP-TSPAN4 were selected with 5 μg/mL puromycin, and 4T1 cells stably expressing GFP-BAF were selected with 5 μg/mL puromycin for a week. Cells were sorted by fluorescence-activated cell sorting (FACS) using a FACS Aria III (BD). The list of chemicals used in this study is provided in Table S4.

CRISPR-Cas9 knockout in hTERT RPE-1 and 4T1 cells

To knock out genes, RPE-1 TP53-/- and 4T1 cells were transfected with pSpCas9-T2A-GFP-2×sgRNA using Lipo8000 (Beyotime, Cat. #C0533). Upon transfection, cells were grown in an antibiotic-free medium for 48 hours, followed by single-cell sorting by FACS Aria III (BD). Single cells were screened for the desired deletion by PCR using primers flanking the targeted exon

regions. All sgRNAs were carefully designed and selected based on predicted low off-target activity using the CRISPOR tool (http://crispor.tefor.net).

To further obtain and validate the knockout clones, genomic DNA of the expanded clones was extracted using a Genomic DNA purification Kit (Thermo Fisher Scientific, Cat. #K0512) for PCR. PCR products were resolved on an agarose gel and purified using PCR gel purification kit (Thermo Fisher Scientific, Cat. #K0701). For TSPAN4 knockout, genotypic analysis was carried out with the ICE tool (https://ice.editco.bio/#/). For TSPAN7 knockout, PCR product was cloned into pMD19-T vector (Takara, Cat. #D102A) by TA cloning according to the manufacturer's instructions. A total of 17 clones were selected for sequencing and subsequent sequence analysis to verify the targeted genetic modifications. The primers used for TSPAN4 and TSPAN7 amplification are listed in Table S3.

Western blot

To assess protein levels, cells and migrasomes were lysed with 80 μL of ice-cold RIPA lysis buffer, supplemented with 1.0 μM PMSF (Sangon Biotech, Cat. #A610425-0005) and 1× protease inhibitor cocktail (MCE, Cat. #HY-K0010), and incubated on ice for 30 min. The lysates were then centrifuged at 20,000 g for 30 min at 4℃. An equal volume of 4× SDS sample buffer (1/3 of the total lysate volume) was added to the supernatant. The samples were boiled for 10 min at 95℃ and immediately subjected to SDS-PAGE gels at 150 V for 75 min. The separated proteins were then transferred to a nitrocellulose (NC) membrane at 100 V for 80 min using a transfer apparatus. The NC membrane was blocked with 5% (w/v) non-fat milk dissolved in 1× TBST buffer for 1 hour at room temperature. Subsequently, the membrane was incubated with primary antibodies overnight at 4℃ on an orbital shaker. After incubation, the membrane was washed three times with 1× TBST buffer or 10 min each at room temperature. The membrane was then incubated with secondary antibodies for 1 h at room temperature with gentle agitation. After removal of the secondary antibody, the NC membrane was washed with 1× TBST buffer for 5 min for three times. Images were acquired using an ECL detection kit (Beyotime, Cat. #P0018FS) or LiCOR Odyssey Imaging System (LiCOR, USA).

The following primary antibodies were used for western blot analyses at the indicated dilution: Rabbit anti-V5 (1:5000, Abcam, Cat. #ab27671), Mouse anti-GAPDH (1:10000, Abcam, Cat. #ab9485). Secondary antibodies used are as follows: HRP-conjugated goat anti-mouse IgG (Sangon Biotech, Cat. #D110087), HRP-conjugated goat anti-rabbit IgG (Sangon Biotech, Cat. #D110058), donkey-anti-rabbit IRDye 680RD (1:10000, LI-OCR, Cat. #926-68073), donkey-anti-mouse IRDye 800CW (1:10000, LI-OCR, Cat. #926-32212).

Immunofluorescence

Cells grown on coverslips were fixed with 4% paraformaldehyde (PFA) for 10 min at room temperature after indicated treatments. After fixation, cells were washed three times with 1× PBS buffer for 5 min at room temperature. Permeabilization was then performed using 1× PBS buffer with 0.5% Triton X-100 at room temperature for 5 min, followed by blocking with 3% BSA in 1× PBS buffer for 1 hour. Cells were incubated with primary antibodies overnight at 4°C. Alexa Fluor 488 or 647-conjugated secondary antibodies (Invitrogen) were applied for 1 h at room temperature. The following primary antibody was used for immunofluorescence at the indicated dilution: Rabbit anti-H2AX p-S139 (1:400, Cell Signaling Technologies, Cat. #2577L).

Purification of migrasomes

Migrasome isolation was performed by iodixanol-sucrose density gradient centrifugation using an Optiprep kit (Sigma-Aldrich, Cat. #LYSISO1). The assay was performed as previously described (*47*). Briefly, TetOn-TRF2-DN RPE-1 cells stably expressing H2B-BFP GFP-BAF and RFP-TSPAN4 were grown in 80× 150 mm dishes precoated with fibronectin (10 μg/mL) in full DMEM medium with 2 μg/mL doxycycline for 48 hours. The growth medium was disposed of and cells were washed to remove other extracellular vesicles in the medium. Cells were trypsinized and collected in 50 mL tubes. All subsequent manipulations were performed at 4℃. Cells and large debris were removed by centrifugation at 1000 g for 10 min followed by 4000 g for 20 min. Crude migrasomes were then collected as the pellet by centrifugation at 18,000 g for 30 min. Migrasome fractionation was performed by density gradient centrifugation, using Optiprep as the density medium. The crude migrasome sample was prepared by resuspending the pellet with 400 μL 1× extraction buffer mixed with 400 μL 10% Optiprep. First, a step gradient was built starting with 50% (500 μL), followed by 40% (500 μL), 35% (500 μL), 30% (500 μL), 25% (500 μL), 20% (500 μL), 15% (500 μL), 10% (500 μL), 5% (500 μL) and crude migrasomes (5%, 800 μL). Second, the prepared gradient was centrifuged at 150,000 g for 4 hours at 4℃ in an MLS-50 rotor (Beckman). Third, samples were collected from top to bottom (500 μL per fraction). Each fraction was mixed with the same volume of 1× PBS buffer (500 μL) and centrifuged at 20,000 g for 30 min to collect the pellet. The pellet was washed with 1× PBS buffer and centrifuged again at 20,000 g for 30 min. Commercial kits used in this study are listed in Table S5.

Wheat germ agglutinin (WGA) staining

For migrasome staining, culture dishes were pre-coated with 10 μg/mL fibronectin prior to cell seeding. After overnight incubation, cells were stained with 1 μg/mL WGA (Thermo Fisher Cat. #W7024) for 30 min and imaged for analysis.

Animal experiments

Four-week-old female BALB/c nude mice, obtained from GemPharmatech Co., Ltd. China, were maintained in a controlled environment with a 12-hour light/dark cycle, constant temperature, and *ad libitum* access to food and water. After a 1-week acclimation period, the mice were randomly assigned to experimental groups. For the *in vivo* tumor model, the mice were anesthetized with isoflurane. Then, 4T1 TetON-TRF2-DN or TSPAN4 KO TetON-TRF2-DN cells (1×10^5 cells per mouse) were subcutaneously injected into the mammary glands of each mouse. Tumor growth was monitored by measuring the tumor length (L) and width (W) using slide calipers every other day, and tumor volume was calculated using the formula: tumor volume (mm^3) = $0.5 \times L \times W^2$. Once the tumor volume reached approximately 100 mm^3, doxycycline (20 mg/kg) was administered orally every other day to induce the expression of TRF2-DN. After 20 days, mice were euthanized, tumor weights were recorded, and tumors were harvested for subsequent analyses. All animal procedures were conducted in accordance with the guidelines approved by the Institutional Animal Care and Use Committee of Shenzhen Bay Laboratory (Approval No. AEDL202201).

Immunohistochemistry (IHC)

For IHC staining, the tumor samples were fixed in 4% PFA and embedded in paraffin, and 8-μm thick sections were stained with WGA at room temperature for 2 hours, followed by staining with Hoechst and examined with a microscope.

Esophageal carcinoma and lymph node metastatic carcinoma tissue chip (DM065Es01), multi-organ tumor and marginal tissue combination chip (X096Mc01) were purchased from Bioaitech Co., Ltd. (Xi'an, China). The study using the tissue microarray was approved by the Life Sciences Ethics Committee of Yaxiang Biotechnology Co., Ltd. (Changsha, China). The Ethics report is available online at yxswll.ccrl.cn. The query code is B81HAQTVB7C3EK. This process had fully informed consent of the patients. The tissue chip was stained with WGA staining and imaged.

Quantification and statistical analysis

Data are presented as the mean ± standard deviation (SD). Statistical significance between two groups was assessed using an unpaired Student's t-test. For comparisons involving more than two groups, one-way analysis of variance (ANOVA) followed by Tukey's multiple comparisons test was employed. Two-way ANOVA was used for in vivo tumor growth analysis, accounting for both treatment conditions and TSPAN4 alterations. All statistical analyses and graph generation were performed using GraphPad Prism 8 software. The software used in this study is shown in Table S6.

References and Notes:

1. L. C. Funk, L. M. Zasadil, B. A. Weaver, Living in CIN: mitotic infidelity and its consequences for tumor promotion and suppression. *Developmental cell* **39**, 638-652 (2016).
2. A. J. Holland, D. W. Cleveland, Losing balance: the origin and impact of aneuploidy in cancer: 'Exploring aneuploidy: the significance of chromosomal imbalance'review series. *Embo Rep* **13**, 501-514 (2012).
3. X. Xu, S. Nowsheen, M. Deng, Exploring the DNA damage response pathway for synthetic lethality. *Genome Instability & Disease* **4**, 98-120 (2023).
4. X. Chen, A. S. Agustinus, J. Li *et al.*, Chromosomal instability as a driver of cancer progression. *Nat Rev Genet* **26**, 31-46 (2025).
5. L. R. Yates, P. J. Campbell, Evolution of the cancer genome. *Nat Rev Genet* **13**, 795-806 (2012).
6. C. Tomasetti, L. Li, B. Vogelstein, Stem cell divisions, somatic mutations, cancer etiology, and cancer prevention. *Science* **355**, 1330-1334 (2017).
7. T. Helleday, S. Eshtad, S. Nik-Zainal, Mechanisms underlying mutational signatures in human cancers. *Nat Rev Genet* **15**, 585-598 (2014).
8. H. Zhang, W. Lu, Y. Zhou *et al.*, Advances in DNA damage induced by environmental chemical carcinogens. *Genome Instability & Disease* **3**, 317-330 (2022).
9. T. Fujiwara, M. Bandi, M. Nitta *et al.*, Cytokinesis failure generating tetraploids promotes tumorigenesis in *p*53-null cells. *Nature* **437**, 1043-1047 (2005).
10. I. T. P.-C. A. o. W. G. Consortium, Pan-cancer analysis of whole genomes. *Nature* **578**, 82-93 (2020).
11. P. Priestley, J. Baber, M. P. Lolkema *et al.*, Pan-cancer whole-genome analyses of metastatic solid tumours. *Nature* **575**, 210-216 (2019).

12. J. Maciejowski, Y. Li, N. Bosco *et al.*, Chromothripsis and kataegis induced by telomere crisis. *Cell* **163**, 1641-1654 (2015).
13. P. J. Stephens, C. D. Greenman, B. Fu *et al.*, Massive genomic rearrangement acquired in a single catastrophic event during cancer development. *Cell* **144**, 27-40 (2011).
14. N. T. Umbreit, C. Z. Zhang, L. D. Lynch *et al.*, Mechanisms generating cancer genome complexity from a single cell division error. *Science* **368**, eaba0712 (2020).
15. M. L. Leibowitz, C. Z. Zhang, D. Pellman, Chromothripsis: a new mechanism for rapid karyotype evolution. *Annu Rev Genet* **49**, 183-211 (2015).
16. K. Krupina, A. Goginashvili, D. W. Cleveland, Scrambling the genome in cancer: causes and consequences of complex chromosome rearrangements. *Nat Rev Genet* **25**, 196-210 (2024).
17. P. J. Stephens, D. J. McBride, M. L. Lin *et al.*, Complex landscapes of somatic rearrangement in human breast cancer genomes. *Nature* **462**, 1005-1010 (2009).
18. M. D. M. Zompit, M. Stucki, Mechanisms of genome stability maintenance during cell division. *DNA repair* **108**, 103215 (2021).
19. H. Jiang, Y. W. Chan, Chromatin bridges: stochastic breakage or regulated resolution? *Trends in genetics : TIG* **40**, 69-82 (2024).
20. G. Ye, Y. He, Y. Zhang *et al.*, Mitotic DNA repair by TMEJ suppresses replication stress-induced nuclear envelope reassembly defect. *Nature Communications* **16**, 8836 (2025).
21. B. Van Steensel, A. Smogorzewska, T. De Lange, TRF2 protects human telomeres from end-to-end fusions. *Cell* **92**, 401-413 (1998).
22. T. De Lange, Shelterin: the protein complex that shapes and safeguards human telomeres. *Genes Dev* **19**, 2100-2110 (2005).
23. S. L. Thompson, D. A. Compton, Chromosome missegregation in human cells arises through specific types of kinetochore–microtubule attachment errors. *Proceedings of the National Academy of Sciences of the United States of America* **108**, 17974-17978 (2011).
24. A. Janssen, M. Van Der Burg, K. Szuhai *et al.*, Chromosome segregation errors as a cause of DNA damage and structural chromosome aberrations. *Science* **333**, 1895-1898 (2011).
25. C. Oscar Sánchez Solorzano, A. Pascual-Montano, A. Sanchez de Diego *et al.*, Chromothripsis: breakage-fusion-bridge over and over again. *Cell cycle* **12**, 2016-2023 (2013).
26. K. Crasta, N. J. Ganem, R. Dagher *et al.*, DNA breaks and chromosome pulverization from errors in mitosis. *Nature* **482**, 53-58 (2012).
27. S. Liu, M. Kwon, M. Mannino *et al.*, Nuclear envelope assembly defects link mitotic errors to chromothripsis. *Nature* **561**, 551-555 (2018).
28. S. Tang, E. Stokasimov, Y. Cui *et al.*, Breakage of cytoplasmic chromosomes by pathological DNA base excision repair. *Nature* **606**, 930-936 (2022).
29. M. Tkach, C. Théry, Communication by extracellular vesicles: where we are and where we need to go. *Cell* **164**, 1226-1232 (2016).
30. R. Kalluri, V. S. LeBleu, The biology, function, and biomedical applications of exosomes. *Science* **367**, eaau6977 (2020).
31. A. Rustom, R. Saffrich, I. Markovic *et al.*, Nanotubular highways for intercellular organelle transport. *Science* **303**, 1007-1010 (2004).
32. R. Chakraborty, T. Nonaka, M. Hasegawa *et al.*, Tunnelling nanotubes between neuronal and microglial cells allow bi-directional transfer of α-Synuclein and mitochondria. *Cell Death Dis* **14**, 329 (2023).

33. L. Ma, Y. Li, J. Peng *et al.*, Discovery of the migrasome, an organelle mediating release of cytoplasmic contents during cell migration. *Cell Res* **25**, 24-38 (2015).
34. H. Jiao, D. Jiang, X. Hu *et al.*, Mitocytosis, a migrasome-mediated mitochondrial quality-control process. *Cell* **184**, 2896-2910 (2021).
35. M. Zhu, Q. Zou, R. Huang *et al.*, Lateral transfer of mRNA and protein by migrasomes modifies the recipient cells. *Cell Res* **31**, 237-240 (2021).
36. D. Jiang, J. He, L. Yu, The migrasome, an organelle for cell-cell communication. *Trends in cell biology* **35**, 205-216 (2025).
37. B. J. Arnold, I. T. Huang, W. P. Hanage, Horizontal gene transfer and adaptive evolution in bacteria. *Nat Rev Microbiol* **20**, 206-218 (2022).
38. A. E. Mammel, E. M. Hatch, Genome instability from nuclear catastrophe and DNA damage. *Semin Cell Dev Biol* **123**, 131-139 (2022).
39. N. Nakazawa, R. Mehrotra, O. Arakawa *et al.*, ICRF-193, an anticancer topoisomerase II inhibitor, induces arched telophase spindles that snap, leading to a ploidy increase in fission yeast. *Genes Cells* **21**, 978-993 (2016).
40. B. M. Gumbiner, Cell adhesion: the molecular basis of tissue architecture and morphogenesis. *Cell* **84**, 345-357 (1996).
41. R. W. Yeo, O. Y. Zhou, B. L. Zhong *et al.*, Chromatin accessibility dynamics of neurogenic niche cells reveal defects in neural stem cell adhesion and migration during aging. *Nature Aging* **3**, 866-893 (2023).
42. N. T. Umbreit, C. Z. Zhang, L. D. Lynch *et al.*, Mechanisms generating cancer genome complexity from a single cell division error. *Science* **368**, (2020).
43. S. Yu, L. Yu, Migrasome biogenesis and functions. *Febs j* **289**, 7246-7254 (2022).
44. D. Wang, L. Yu, Migrasome biogenesis: when biochemistry meets biophysics on membranes. *Trends Biochem Sci* **49**, 829-840 (2024).
45. J. B. Kim, J.-E. Bae, N. Y. Park *et al.*, TAAR8 Mediates Increased Migrasome Formation by Cadaverine in RPE Cells. *Curr Issues Mol Biol* **46**, 8658-8664 (2024).
46. Y. Huang, B. Zucker, S. Zhang *et al.*, Migrasome formation is mediated by assembly of micron-scale tetraspanin macrodomains. *Nat Cell Biol* **21**, 991-1002 (2019).
47. D. Jiang, Y. Li, L. Yu, Detection, purification, characterization, and manipulation of migrasomes. *Curr Protoc* **3**, e856 (2023).
48. Y. Dong, X. Tang, W. Zhao *et al.*, TSPAN4 influences glioblastoma progression through regulating EGFR stability. *Iscience* **27**, (2024).
49. L. Chen, L. Ma, L. Yu, WGA is a probe for migrasomes. *Cell discovery* **5**, 13 (2019).
50. C.-Z. Zhang, A. Spektor, H. Cornils *et al.*, Chromothripsis from DNA damage in micronuclei. *Nature* **522**, 179-184 (2015).
51. M. Zhu, Q. Zou, R. Huang *et al.*, Lateral transfer of mRNA and protein by migrasomes modifies the recipient cells. *Cell research* **31**, 237-240 (2021).
52. Z. Zhang, C. Zhang, Regulation of cGAS – STING signalling and its diversity of cellular outcomes. *Nature Reviews Immunology*, 1-20 (2025).
53. A. Aguilera, B. Gómez-González, Genome instability: a mechanistic view of its causes and consequences. *Nature Reviews Genetics* **9**, 204-217 (2008).
54. J. T. Lange, J. C. Rose, C. Y. Chen *et al.*, The evolutionary dynamics of extrachromosomal DNA in human cancers. *Nature Genetics* **54**, 1527-1533 (2022).
55. J. Luebeck, A. W. T. Ng, P. C. Galipeau *et al.*, Extrachromosomal DNA in the cancerous transformation of Barrett's oesophagus. *Nature* **616**, 798-805 (2023).

Acknowledgments:

We thank members of the Deng and Ji laboratories for helpful discussions. We thank Dr. Jing Wang at Shenzhen Bay Laboratory and Dr. Yisui Xia at Shenzhen University for the critical reading of the manuscript. We thank Shuonan Wang at Xi'an Jiaotong University, Shuya Han, Fuhai Liu and Haoyue Zhang at Shenzhen Bay Laboratory, Yanfang Tu and Wei Wang from Shenzhen BJR Biomedical Tech, the Bio-imaging Core Facility and the Animal Core Facility at Shenzhen Bay Laboratory for technical helps.

Funding:

National Key R&D Program of China (2022YFA1302800) to LD

Shenzhen Medical Research Funds (B2301007) to LD

National Natural Science Foundation of China (32270779) to LD

Guangdong Special Support Plan (2023TQ07A226) to LD

Proof of Concept Fund of Shenzhen Bay Laboratory (C1022426003) to LD

Shenzhen Bay Laboratory Start-up Fund (S201100001) to LD

National Natural Science Foundation of China (92354304; 32371343; 32122025) to WJ

Shenzhen Bay Scholars Program (S229100002) to WJ

Spark Trial Program from Shenzhen BJR Biomedical Tech to YL

National Natural Science Foundation of China (22207131) to YDH

Author contributions:

Conceptualization: LD

Methodology: YL, CL, GY, YT, YWH, LD

Investigation: YL, CL, GY, YT

Visualization: LD, YL, CL, WC, WJ, CS

Funding acquisition: LD, WJ, YDH, YL

Project administration: WC, YDH, LD

Supervision: LD

Writing – original draft: LD, CL, YL, YT, GY

Competing interests:

Authors declare that they have no competing interests.

Data and materials availability:

Correspondence and requests for materials should be addressed to Dr. Lin Deng. The sequencing data have been deposited in the Gene Expression Omnibus (GEO) under accession number GSE297083.

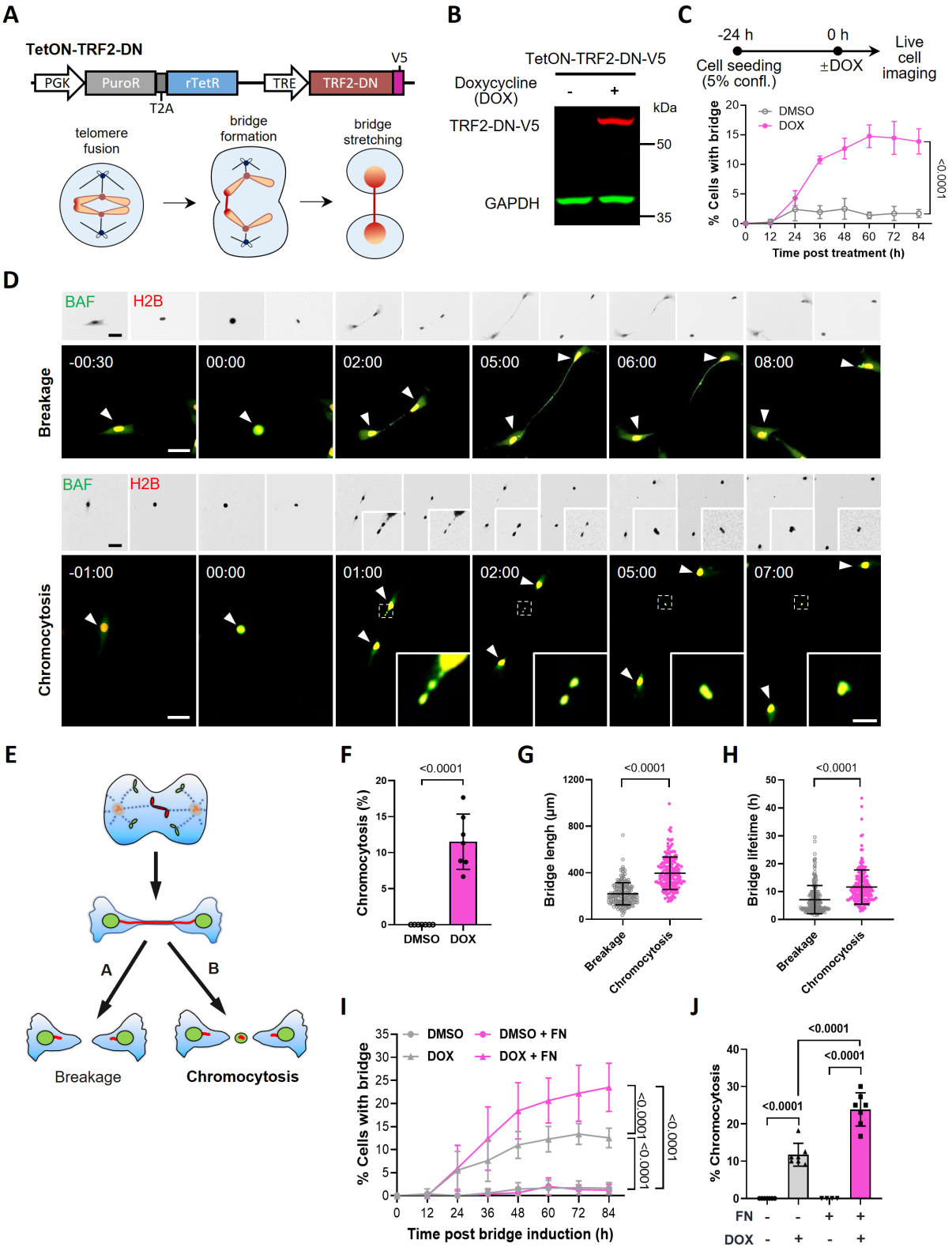

604

Fig. 1. The breakage of chromosome bridges triggers chromocytosis.

(A) Schematic of chromosome bridge formation induced by TRF2-DN expression. TRF2-DN expression disrupted telomere capping, causing chromosome end fusion (red). Spindle tension during late mitosis stretched the fused dicentric chromosomes, forming bridges.

(B) Western blot analysis of TRF2-DN-V5 expression in RPE-1 cells with or without DOX treatment.

(C) Quantification of chromosome bridge formation over time following TRF2-DN induction. Chromosome bridges were visualized using GFP-BAF. Data are presented as mean ± SD, n=4 independent experiments, N>50 for each experiment; The *p* value is calculated by two-way ANOVA with Tukey's multiple comparisons test.

(D) Time-lapse imaging of chromosome bridge (top panels, see movie S1) and chromocytosis (bottom panels, see movie S2) in DOX-treated RPE-1 *TetON-TRF2-DN TP53-/-* cells. GFP-BAF and RFP-H2B were stably expressed and imaged at 20-min intervals. Metaphase was referred to as time "00:00" in hh:mm format due to its round morphology. White arrowheads indicate cell bodies, with insets highlighting extracellular chromatin fragments. Scale bar, 40 μm (original), 10 μm (inset).

(E) Schematic representation of chromsome bridge breakage and chromocytosis for panel D.

(F) Quantification of chromocytosis frequency after TRF2-DN induction. Data are presented as mean ± SD, n=7 independent experiments, N>50 for each experiment; The *p* value is calculated by two-tailed unpaired Student's *t*-test.

(G-H) Quantification of chromosome bridge length (G) and duration/lifetime (H) during simple bridge breakage and chromocytosis. Data are presented as mean ± SD, N>200; The *p* values are calculated by two-tailed unpaired Student's *t*-test.

(I) Quantification of chromosome bridge formation in RPE-1 cells treated with DMSO or DOX for 84 hours, with or without fibronectin (FN) coating. Data are presented as mean ± SD, n>3 independent experiments, N>50 for each experiment; The *p* values are from two-way ANOVA with Tukey's multiple comparisons test.

(J) Quantification of chromocytosis in (I), presented as mean ± SD, n=6 independent experiments, N>50 per experiment; The *p* values from two-tailed unpaired Student's *t*-test are labeled for interested pairs.

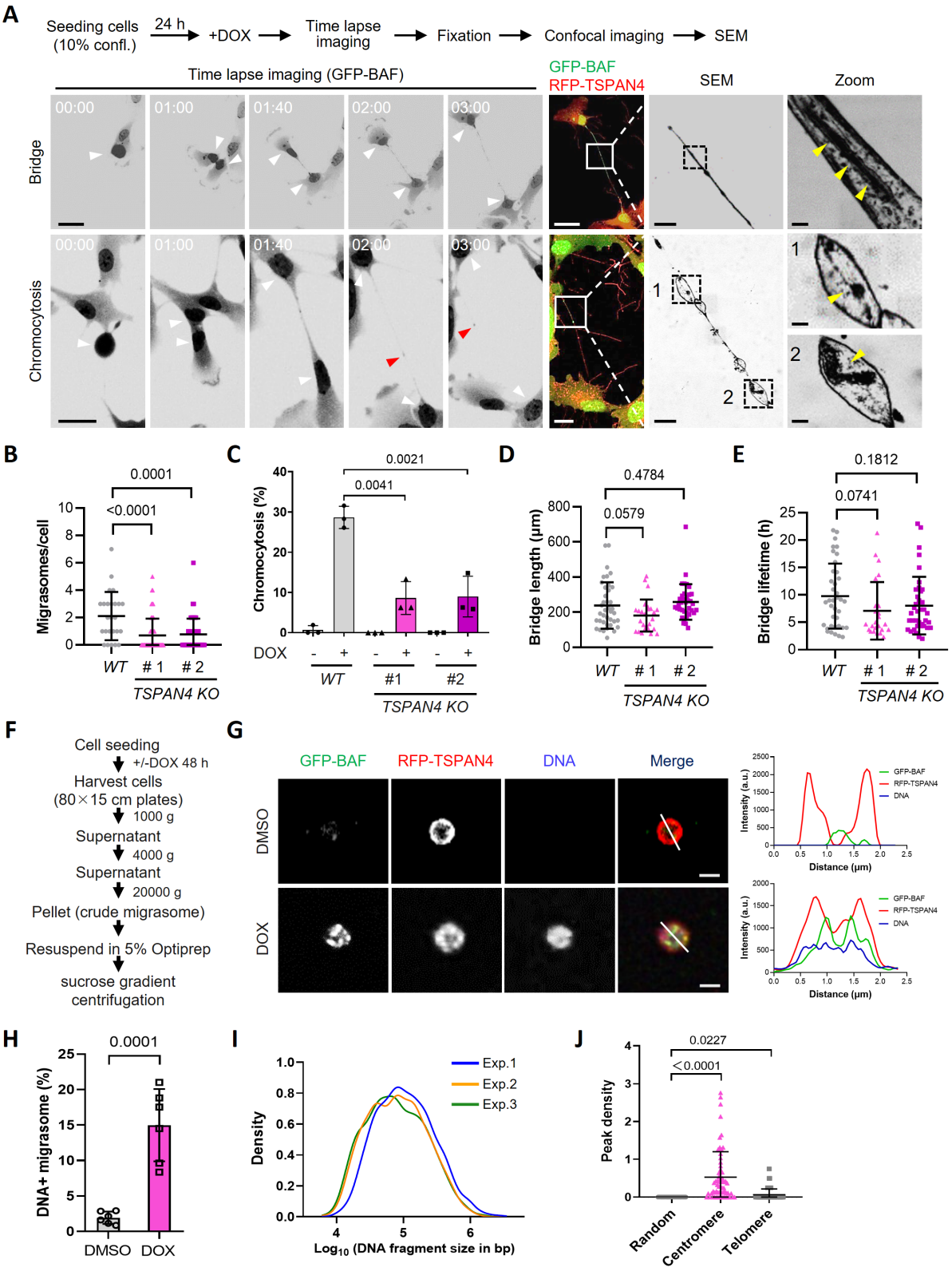

Fig. 2. Migrasomes are required for chromocytosis.

(A) Representative CLEM images illustrating chromosome bridges (top panels, see movie S7) and chromocytosis (bottom panels, see movie S8). Time-lapse imaging captured the progression of chromosome bridges and chromocytosis prior to sample fixation for confocal imaging and CLEM. Metaphase was referred to as time "00:00" in hh:mm format due to its round morphology. White arrowheads indicate cell bodies, red arrowheads highlight the chromocytotic DNA fragments, and yellow arrowheads indicate chromatin. Magnified SEM images of boxed regions are shown adjacent to confocal images. Scale bars, 20 μm (confocal), 1 μm (SEM) and 200 nm (Zoom).

(B) Quantification of migrasomes in RPE-1 *WT* and *TSPAN4 KO* clones for fig. S4D. Data are shown as mean ± SD, N>20; The *p* values are from two-tailed unpaired Student's *t*-test.

(C) Quantification of chromocytosis frequency in RPE-1 *WT* and *TSPAN4 KO* clones with or without TRF2-DN induction. Data are presented as mean ± SD, n=3 independent experiments, N>50 for each experiment; The *p* values are from two-tailed unpaired Student's *t*-test.

(D-E) Quantification of chromosome bridge length (D) and lifetime (E) during chromocytosis for RPE-1 *WT* and *TSPAN4 KO* clones. Data are shown as mean ± SD, N>30; The *p* values are from two-tailed unpaired Student's *t*-test.

(F) Experimental workflow for migrasome purification for confocal imaging, and sequencing analysis.

(G) Representative images of migrasomes purified from RPE-1 cells stably expressing GFP-BAF RFP-TSPAN4 without (DMSO) or with TRF2-DN (DOX) induction (left). Scale bar, 1 μm. Right: line-scan intensity profiles along the white line in merged images.

(H) Quantification of migrasomes positive for DNA. Data are presented as mean ± SD, n=6 independent experiments, N>100 for each experiment; The *p* value is from two-tailed unpaired Student's *t*-test.

(I) The distributions of fragment size of chromocytotic DNA from three independent experiments.

(J) Positional bias analysis for chromocytotic DNA peaks. Chromosome regions were classified as centromere, telomere and random regions. n=3 independent experiments. Data are presented as mean ± SD; The *p* values are from Wilcoxon test.

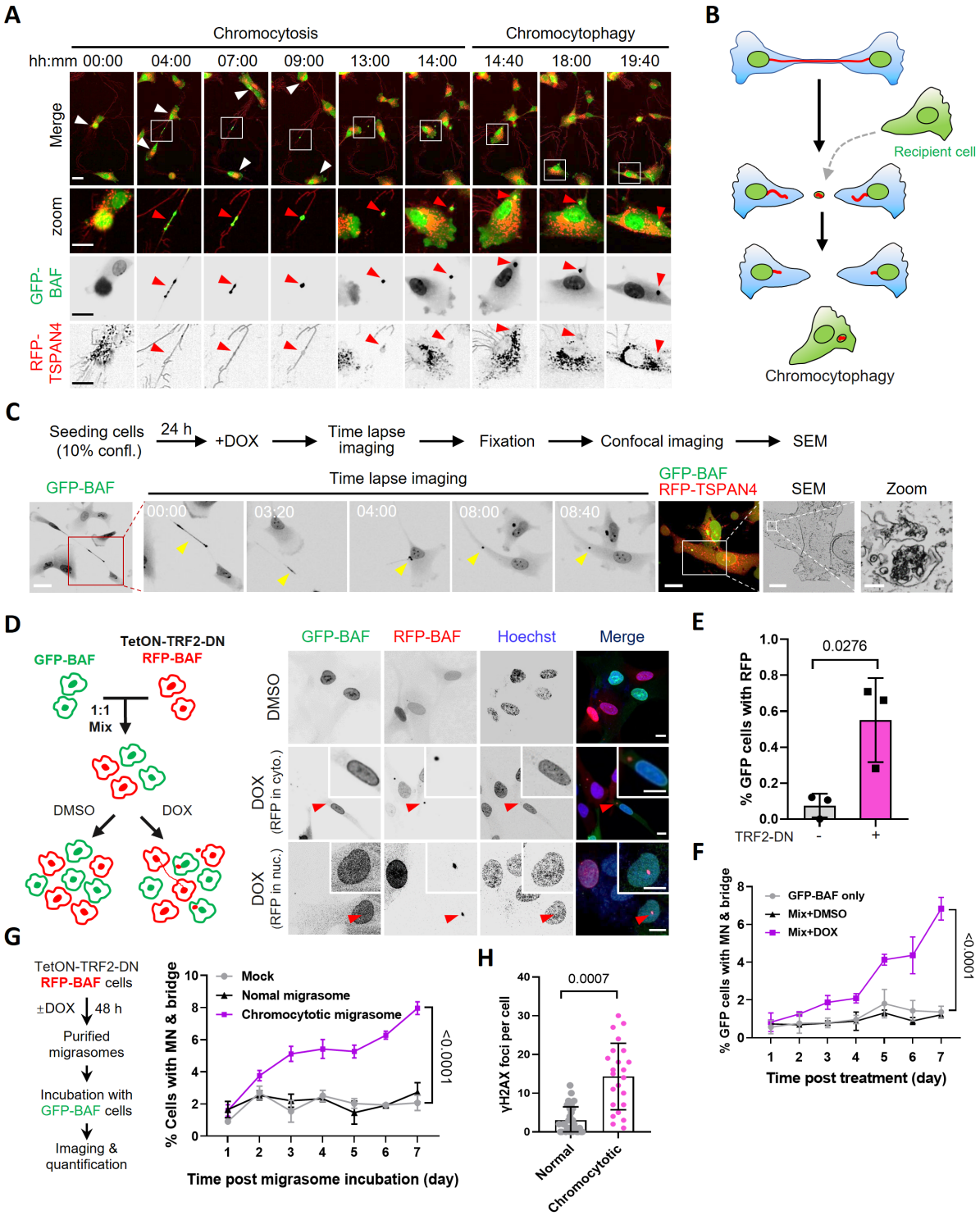

665

Fig. 3. Intercellular transfer of chromocytotic DNA causes genome instability.

(A) Time-lapse imaging of chromosome bridges (GFP-BAF) and migrasomes (RFP-TSPAN4), with 20 min intervals (see movie S10). Metaphase was set as "00:00" in hh:mm format. White arrowheads indicate cell bodies; red arrowheads highlight chromocytotic DNA fragments. Insets display magnified views of chromocytotic DNA and migrasome. Scale bar, 50 μm.

(B) Schematic representation of chromocytophagy for panel **A**.

(C) Representative CLEM images depicting chromocytophagy. Time-lapse imaging, in hh:mm format, captured the progression of chromocytophagy prior to sample fixation for confocal imaging and CLEM (see movie S12). Yellow arrowheads indicate chromatin fragments. Magnified SEM images of the highlighted boxed regions are displayed adjacent to the corresponding confocal images. Scale bars, 20 μm (confocal), 10 μm (SEM) and 200 nm (Zoom).

(D) Validation of intercellular chromatin transfer by co-culturing GFP-BAF cells with RFP-BAF TetON-TRF2-DN cells. Red arrowheads denote the chromocytotic DNA fragment (RFP-BAF) in recipient cells (GFP-BAF) after DOX treatment for 48 hours. Red arrowheads denote chromocytotic fragments. Scale bar, 10 μm.

(E) Quantification of intercellular chromatin transfer for panel D. Data are presented as mean ± SD, n=3 independent experiments, N>100 for each experiment; two-tailed unpaired Student's *t*-test.

(F) Quantification of micronuclei (MN) and chromosome bridges in GFP-BAF cells for 7 days post DOX treatment. The GFP-BAF cells without co-culturing (GFP-BAF only) were included to assess the baseline. Data are presented as mean ± SD, n=3 independent experiments, N>300 for each experiment; The *p* value is from two-tailed unpaired Student's *t*-test.

(G) The effect of purified migrasomes from indicated conditions on GFP-BAF cells. Micronuclei and chromosome bridges in GFP-BAF cells were quantified for 7 days after incubation with migrasomes. Mock (buffer treatment) was included to assess the baseline. Data are presented as mean ± SD, n=3 independent experiments, N>300 for each experiment; the *p* value is from two-way ANOVA with Tukey's multiple comparisons test.

(H) Quantification of γH2AX foci in GFP-BAF cells incubated with normal migrasomes or migrasomes with chromocytotic DNA. Data are presented as mean ± SD, n=3 independent experiments, N>20; the *p* value is from two-tailed unpaired Student's *t*-test.

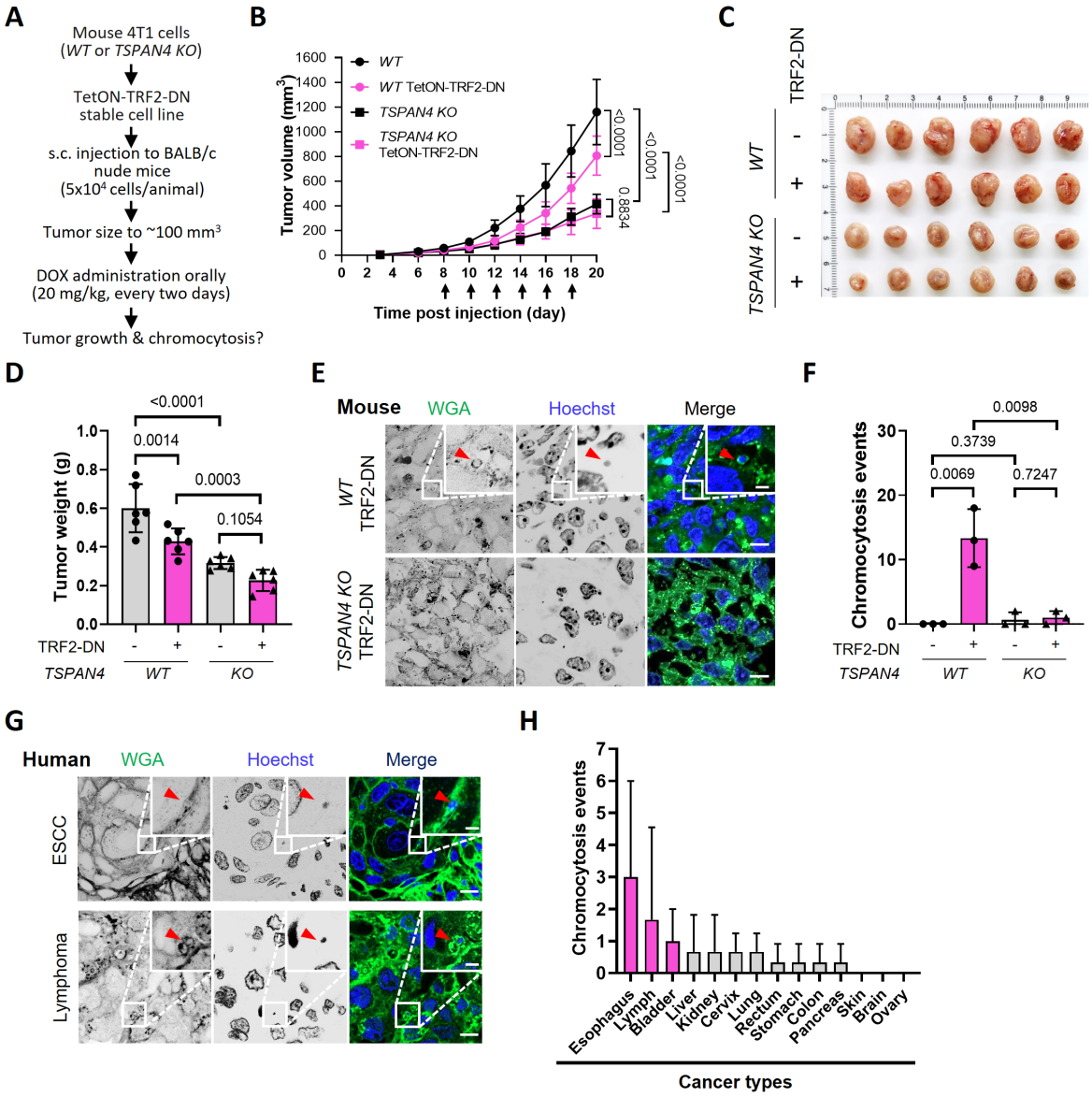

696

Fig. 4. Chromocytosis occurs in mouse tumor models and human clinical samples.

(A) Experimental workflow for assessing tumor growth and chromocytosis. Mouse 4T1 *WT* and *TSPAN4 KO* cells with or without TetON-TRF2-DN were subcutaneously injected into the mammary glands of immunodeficient female BALB/c nude mice. DOX was administered orally to induce TRF2-DN expression.

(B) Quantification of tumor growth. The black arrows at the bottom denote DOX treatments. Data are presented as mean ± SD, N=6; The *p* values are from two-way ANOVA with Tukey's multiple comparisons test.

(C-D) Imaging (C) and quantification (D) of the indicated mouse tumors harvested on day 20 post-injection. Data are presented as mean ± SD, N=6; The *p* values from two-tailed unpaired Student's *t*-test are labeled for interested pairs.

(E) Representative images of tumor sections with DAPI and WGA staining. Red arrowheads indicate potential chromocytotic DNA. Scale bar, 10 μm.

(F) Quantification of chromocytosis events in mouse tumor samples in panel E. Data are presented as mean ± SD, n=3 independent experiments; The *p* values from two-tailed unpaired Student's *t*-test are indicated for interested pairs.

(G) Representative images of human ESCC and lymphoma sections from tissue microarrays with DAPI and WGA staining. Red arrowheads indicate potential events of chromocytosis. Scale bar, 10 μm.

(H) Quantification of chromocytosis events in different human cancer types. Data are presented as mean ± SD, N=3.